

# Linear Perturbation constraints on Multi-coupled Dark Energy

Arpine Piloyan,<sup>a</sup> Valerio Marra,<sup>b</sup> Marco Baldi<sup>c,d,e</sup> and Luca Amendola<sup>b</sup>

<sup>a</sup>Yerevan State University, Alex Manoogian 1, Yerevan 0025, Armenia;

<sup>b</sup>Institut für Theoretische Physik, Universität Heidelberg, Philosophenweg 16, 69120 Heidelberg, Germany;

<sup>c</sup>Dipartimento di Fisica e Astronomia, Università di Bologna, Viale C. Berti-Pichat 6/2, I-40127 Bologna, Italy;

<sup>d</sup>INAF, Osservatorio Astronomico di Bologna, Viale C. Berti-Pichat 6/2, I-40127 Bologna, Italy;

<sup>e</sup>INFN - Sezione di Bologna, Viale C. Berti Pichat 6/2, I-40127 Bologna, Italy.

**Abstract.** The Multi-coupled Dark Energy (McDE) scenario has been recently proposed as a specific example of a cosmological model characterized by a non-standard physics of the dark sector of the universe that nevertheless gives an expansion history which does not significantly differ from the one of the standard  $\Lambda$ CDM model. Thanks to a dynamical screening mechanism, in fact, the interaction between the Dark Energy field and the Dark Matter sector is effectively suppressed at the background level during matter domination. As a consequence, background observables cannot discriminate a McDE cosmology from  $\Lambda$ CDM for a wide range of model parameters. On the other hand, linear perturbations are expected to provide tighter bounds due to the existence of attractive and repulsive fifth-forces associated with the dark interactions. In this work, we present the first constraints on the McDE scenario obtained by comparing the predicted evolution of linear density perturbations with a large compilation of recent data sets for the growth rate  $f\sigma_8$ , including 6dFGS, LRG, BOSS, WiggleZ and VIPERS. Confirming qualitative expectations, growth rate data provide much tighter bounds on the model parameters as compared to the extremely loose bounds that can be obtained when only the background expansion history is considered. In particular, the 95% confidence level on the coupling strength  $|\beta|$  is reduced from  $|\beta| \leq 83$  (background constraints only) to  $|\beta| \leq 0.88$  (background and linear perturbation constraints). We also investigate how these constraints further improve when using data from future wide-field surveys such as supernova data from LSST and growth rate data from Euclid-type missions. In this case the 95% confidence level on the coupling further reduce to  $|\beta| \leq 0.85$ . Such constraints are in any case still consistent with a scalar fifth-force of gravitational strength, and we foresee that tighter bounds might be possibly obtained from the investigation of nonlinear structure formation in McDE cosmologies.

**Keywords:** dark energy theory, cosmological perturbation theory

---

## Contents

<b>1</b>	<b>Introduction</b>	<b>1</b>
<b>2</b>	<b>Linear perturbation equations</b>	<b>3</b>
<b>3</b>	<b>Analytical solutions of the perturbation equations</b>	<b>4</b>
<b>4</b>	<b>Numerical solutions of the perturbation equations</b>	<b>5</b>
<b>5</b>	<b>Comparison to observations</b>	<b>9</b>
5.1	SN data	10
5.2	$f\sigma_8(z)$ data	11
5.3	Full likelihood	11
<b>6</b>	<b>Results</b>	<b>12</b>
<b>7</b>	<b>Conclusions</b>	<b>13</b>
<b>A</b>	<b>Including a baryonic component</b>	<b>14</b>
A.1	Equations	14
A.2	Results	15

---

## 1 Introduction

Understanding the fundamental origin of the observed accelerated expansion of the Universe [1–4] represents the driving scientific case for a large number of complex and ambitious international initiatives planned for the next decade of cosmological observations, including e.g. the Baryon Oscillation Spectroscopic Survey [BOSS, 5], the Dark Energy Survey [DES, 6], the Large Synoptic Space Telescope [LSST, 7] and the ESA satellite mission Euclid<sup>1</sup> [8]. Besides an exquisite quality of observational data and a rigorous control of any possible systematics, such a challenging task will also require reliable predictions of how different theoretical scenarios might be scrutinised and possibly disentangled by efficiently combining different observational probes. More specifically, in order to discriminate a wide variety of Dark Energy (DE) or Modified Gravity (MG) models from the standard cosmological constant – presently assumed as the fiducial scenario – an appropriate combination of geometrical and dynamical observables is generally required, as competing models often feature strong degeneracies with the standard cosmological parameters when single observational probes are considered.

In this respect, it is particularly instructive to investigate cosmological scenarios that are practically indistinguishable from the fiducial  $\Lambda$ CDM model as far as some particular observational probes are concerned, while showing characteristic features through other observational channels. While the most widely investigated alternatives to the cosmological constant such as *Quintessence* [9, 10], *k-essence* [11], *phantom* [12] and *quintom* [13] DE models, or more complex scenarios like *interacting DE* [14–17], *the Growing Neutrino model* [18] and generic MG theories [as proposed e.g. by 19–24] generally affect both the background and linear perturbations evolution of the universe, some specific

---

<sup>1</sup>[www.euclid-ec.org](http://www.euclid-ec.org)

realisations of these models were found to have the appealing (and challenging) feature of sharing the same expansion history of the  $\Lambda$ CDM cosmology to an extreme level of precision. Such models – which include e.g. the Hu & Sawicki realisation of  $f(R)$  theories [21] and the Multi-coupled Dark Energy (McDE) scenario [25] discussed in the present work – represent an ideal benchmark to test the predictive power of future multi-probe observational surveys.

In particular, the McDE model was proposed as a particular realisation of the more general framework discussed by Ref. [26] with the aim of providing an extension to the standard coupled Dark Energy (cDE) scenario in terms of a multi-particle nature of the CDM field, without introducing additional free parameters. In fact, the McDE model discussed in the present work is characterised by a hidden symmetry in the CDM sector associated with two distinct particle species with opposite couplings to a single DE scalar field, thereby requiring the same number of free parameters (a self-interaction potential slope  $\alpha$  and a coupling constant  $\beta$ ) as the widely investigated coupled Quintessence models. However, differently from the latter, the CDM internal symmetry that characterises McDE scenarios has been shown to provide a self-regulating mechanism of the effective interaction strength, thereby very effectively suppressing the DE-CDM interaction at the background level.

Such background screening of the DE-CDM interaction has been qualitatively demonstrated by [25] and subsequently investigated in full detail by our team in [27]. In the latter paper, we provided the first direct comparison of McDE cosmologies with real observational data consisting of the supernova luminosities of the publicly available Union2.1 sample [28]. Confirming the previous qualitative results of [25], our analysis directly showed how present observational data on the background expansion history of the Universe are fully consistent with McDE scenarios even for very large values of the DE coupling, up to three orders of magnitude larger than the present bounds on the coupling for standard cDE models ( $\beta \lesssim 0.1$ , see e.g. [29, 30]). In fact, the conclusion of our previous paper was that the background dynamics could hardly offer any significant constraint on the McDE model and anticipated that more severe constraints could be obtained by working out the behavior of perturbations.

This paper is devoted to such a task. Our primary goal is to derive observational constraints on the main parameters of the McDE model based on the latest available data on the growth of linear density perturbations, with the aim to significantly improve the extremely loose bounds derived through background observables, thereby reducing the viable parameter space. This task is also particularly relevant in view of the further extension of the investigation of the McDE scenario to the nonlinear regime of structure formation by means of dedicated N-body simulations. As the latter are in general quite computationally expensive, especially for large values of the coupling, constraining the viable region of the model’s parameter space through linear observables will avoid wasting precious computational resources. To this end, we will first derive the full set of linear perturbation equations in the McDE model and we will analytically solve them for the simplified cases of the background critical points in phase space. Then, we will integrate numerically the equations to obtain the full solution and check the analytical results. With the full numerical evolution of the linear perturbation growth at hand, we will finally compare the predictions obtained for different choices of model parameters with our sample of observational data by performing a detailed sampling of the parameter space. Our final result will be marginalised posterior bounds. As we will discuss below, such a procedure provides the most stringent constraints to date on this type of cosmological models.

The paper is organised as follows. In Section 2 we introduce the full system of linear perturbation equations for the McDE scenario, in Section 3 we derive analytical solutions for the background critical points that determine a viable cosmological expansion history, and in Section 4 we compute the full numerical solutions of the system. In Section 5 we present the datasets adopted for our anal-

ysis and we describe the procedure for the direct comparison with observational data. In Section 6 we discuss the main results of our work and provide observational constraints on the McDE parameters. Finally, in Section 7 we conclude. Furthermore, in Appendix A we consider the effect of the uncoupled baryonic component showing that this does not significantly affect our main results.

## 2 Linear perturbation equations

The McDE model, proposed and investigated by [25, 27, 31], is characterised by the existence of two different species of CDM particles with opposite couplings to the same classical DE scalar field. The system is therefore described by the following Lagrangian:

$$S = \int d^4x \sqrt{-g} \left[ \frac{M_{Pl}^2}{2} R - \frac{1}{2} \phi^{;\alpha} \phi_{;\alpha} - \sum_{\pm} m_{\pm} e^{\pm \sqrt{\frac{2}{3}} \frac{\beta}{M_{Pl}} \phi} \bar{\psi}_{\pm} \psi_{\pm} - V(\phi) + \mathcal{L}_r \right], \quad (2.1)$$

where  $\phi$  is the dark energy scalar field,  $\psi_{\pm}$  represent the two CDM fields,  $\beta$  is a dimensionless parameter defining the strength of the interaction, and  $\mathcal{L}_r$  is the radiation Lagrangian. In eq. (2.1) we have discarded the uncoupled baryonic component as its contribution does not significantly alter the results of our analysis. However, in the Appendix A we will drop this assumption and properly quantify the effect of baryons on our results. As we will see, these have a rather small impact, due to the low baryonic density observed today, which makes our simplified setup fully justified.

We restrict our attention to a spatially flat FLRW metric. Perturbation equations corresponding to the model of eq. (2.1) on sub-horizon scales for each species of dark matter have been derived in [25] and read:

$$\ddot{\delta}_{-} = -2H \left( 1 + \beta \frac{\dot{\phi}}{\sqrt{6}H} \right) \dot{\delta}_{-} + 4\pi G (\rho_{-} \Gamma_A \delta_{-} + \rho_{+} \Gamma_R \delta_{+}), \quad (2.2)$$

$$\ddot{\delta}_{+} = -2H \left( 1 - \beta \frac{\dot{\phi}}{\sqrt{6}H} \right) \dot{\delta}_{+} + 4\pi G (\rho_{-} \delta_{-} \Gamma_R + \rho_{+} \delta_{+} \Gamma_A), \quad (2.3)$$

where  $\rho_{\pm}$  are the energy densities of the two CDM species,  $\delta_{\pm}$  their respective density contrasts, and where the  $\Gamma$  factors

$$\Gamma_R = 1 - \frac{4}{3} \beta^2, \quad (2.4)$$

$$\Gamma_A = 1 + \frac{4}{3} \beta^2 \quad (2.5)$$

encode the effects of repulsive ( $R$ ) and attractive ( $A$ ) fifth-forces.

It is convenient to rewrite these equations employing the  $e$ -folding  $N$  as the time variable,  $N \equiv \ln a$ , and to introduce the following dimensionless quantities:

$$x^2 \equiv \frac{\dot{\phi}^2}{6M_{Pl}^2 H^2}, \quad y^2 \equiv \frac{V}{3M_{Pl}^2 H^2}, \quad (2.6)$$

$$z_{\pm}^2 \equiv \frac{\rho_{\pm}}{3M_{Pl}^2 H^2}, \quad r^2 \equiv \frac{\rho_r}{3M_{Pl}^2 H^2}. \quad (2.7)$$

The linear perturbations equations with respect to  $N$  then read

$$\delta_{-}'' + \left[ 2(1 + \beta x) - \frac{1}{2}(3 - 3y^2 + 3x^2 + r^2) \right] \delta_{-}' = \frac{3}{2} (z_{-}^2 \Gamma_A \delta_{-} + z_{+}^2 \Gamma_R \delta_{+}), \quad (2.8)$$

$$\delta_{+}'' + \left[ 2(1 - \beta x) - \frac{1}{2}(3 - 3y^2 + 3x^2 + r^2) \right] \delta_{+}' = \frac{3}{2} (z_{-}^2 \Gamma_R \delta_{-} + z_{+}^2 \delta_{+} \Gamma_A), \quad (2.9)$$

Point	$x$	$y$	$z_+$	$z_-$	$\Omega_{\text{DE}}$	$w_{\text{eff}}$	$\mu$
1	$\pm 1$	0	0	0	1	1	0
2	$\frac{\alpha}{3}$	$\frac{1}{3}\sqrt{9-\alpha^2}$	0	0	1	$-1 + \frac{2\alpha^2}{9}$	0
3	0	0	$\frac{1}{\sqrt{2}}$	$\frac{1}{\sqrt{2}}$	0	0	0
4	$-\frac{2\beta}{3}$	0	$\sqrt{1 - \frac{4\beta^2}{9}}$	0	$\frac{4\beta^2}{9}$	$\frac{4\beta^2}{9}$	1
5	$\frac{3}{2(\alpha+\beta)}$	$\frac{\sqrt{9+4\alpha\beta+4\beta^2}}{2 \alpha+\beta }$	$\frac{\sqrt{-9+2\alpha\beta+2\alpha^2}}{\sqrt{2} \alpha+\beta }$	0	$\frac{9+2\alpha\beta+2\beta^2}{2(\alpha+\beta)^2}$	$\frac{-\beta}{(\alpha+\beta)}$	1

**Table 1.** Critical points for background equations provided in [27]. Only the physical solutions for  $x, y, z_+, z_-$  are selected. Only points 2 and 5 can have accelerated expansion ( $w_{\text{eff}} < -1/3$ ).

where we have made use of the background equation

$$\frac{H'}{H} = -\frac{1}{2}(3 - 3y^2 + 3x^2 + r^2). \quad (2.10)$$

The background behavior was studied and compared to observations in [27], where it was shown that the background evolution on a spatially flat FLRW metric is characterized by several critical-points defined as solutions for which  $x, y, z_{\pm}$  are constant. These are summarised in Table 1. Among these, two critical points (point 2 and point 5) represent accelerated stable solutions, and two are metastable (saddle points) matter-dominated solutions (point 3 and point 4): viable cosmologies should connect one of the two matter eras to one of the two accelerated regimes. As points 3 and 4 are metastable points, their occurrence strongly depends on the initial conditions; the occurrence of the stable points, on the contrary, depends only on the values of the parameters  $\alpha, \beta$ . Therefore, by choosing the parameters in the appropriate range we will obtain either point 2 (in which dark energy dominates) or 5 (in which dark energy and dark matter coexist) as final state. The metastable matter eras will instead generally both occur for the same parameters, one after the other. However, point 3 will always be the last point before dark energy domination, since the matter density dilutes more slowly for point 3 than for point 4 (i.e. the equation of state is smaller for point 3, see Table 1). Therefore, if the initial conditions are set far enough in the past we expect the phase relative to point 4 to end very early and not to affect the late-time observations (supernovae and growth rate) considered in this work. In the following we will therefore always assume that we can neglect the possible point 4 matter era.

In the next Sections we will first solve the perturbation equations analytically on the background critical points, and then numerically along the full trajectory.

### 3 Analytical solutions of the perturbation equations

On the particular background solutions corresponding to the critical points of Table 1, the perturbation equations become constant-coefficient linear equations and, therefore, exactly solvable. Thus, the analytical solutions of perturbations on the background critical points will approximate the full solutions in the matter era (point 3) and final accelerated stage (point 2 or point 5), respectively, as shown in the following sections. We define the total matter perturbation as:

$$\delta = \frac{\Omega_- \delta_- + \Omega_+ \delta_+}{\Omega_- + \Omega_+}, \quad (3.1)$$

and, correspondingly, the total and partial growth rates as:

$$f = \frac{\delta'}{\delta}, \quad f_{\pm} = \frac{\delta'_{\pm}}{\delta_{\pm}}. \quad (3.2)$$

We consider only one quadrant of the parameter plane,  $\{\alpha > 0, \beta > 0\}$ , since due to the symmetry of the system it is sufficient to solve equations with positive values of parameters. Indeed, the sign of the coupling is completely irrelevant and all our constraints will refer to its absolute value  $|\beta|$ . The analytical solutions of eq. (2.8) are presented in Table 2 for each of the five critical points. Only the growing solutions of the dark matter components and total density perturbation,  $f_{\pm}$ ,  $f$ , respectively, are selected. For point 3 the perturbations  $\delta_+$  and  $\delta_-$  have opposite signs and compensate each other so that the total growth function  $f$  is always unity. Nonetheless, near the transition between point 3 and point 2 (or point 5) the symmetry between the background densities of the two CDM species, that is ensured by the matter-dominated attractor, starts to be violated, which gives rise to the solution  $f = f_- + 3$  in this region. This can be justified if we write  $f$  in more detail, as:

$$\begin{aligned} f &= \frac{\delta'}{\delta} = \left[ \frac{\Omega_- \delta_- + \Omega_+ \delta_+}{\Omega_- + \Omega_+} \right]' / \left[ \frac{\Omega_- \delta_- + \Omega_+ \delta_+}{\Omega_- + \Omega_+} \right] \\ &= \frac{\Omega_- \delta'_- + \Omega_+ \delta'_+}{\Omega_- \delta_- + \Omega_+ \delta_+} + \frac{\Omega'_- \delta_- + \Omega'_+ \delta_+}{\Omega_- \delta_- + \Omega_+ \delta_+} - \frac{\Omega'_- + \Omega'_+}{\Omega_- + \Omega_+}. \end{aligned} \quad (3.3)$$

At point 3, the first term on the second line of eq. (3.3) is unity as long as  $\Omega_- \delta_-$  and  $\Omega_+ \delta_+$  exactly compensate each other. However, as soon as  $\Omega_- \neq \Omega_+$  (i.e. when the system is about to move out of point 3) it behaves as  $f_-$ . In this case the second term is also different from zero. In fact, analytical calculations show that  $\Omega_- - \Omega_+ \sim e^{3N}$  when the system is about to go out of point 3, which leads to:

$$\frac{\Omega'_- \delta_- + \Omega'_+ \delta_+}{\Omega_- \delta_- + \Omega_+ \delta_+} \rightarrow 3, \quad (3.4)$$

as  $\delta_- \approx -\delta_+$ . Finally, the last term is zero at each critical point. It is important to mention that the growth function  $f$  passes through a singularity as the total perturbation  $\delta$  goes through zero. However, the observable is  $\delta'/\delta_0$  (see eq. (5.6)), which is never singular.

For a more complete picture, we present the contour plots of the growth functions for point 2 and point 5 in the left and right panels of Fig. 1, respectively. From these contour plots we conclude that larger values of the McDE characteristic parameters correspond to larger growth rates; moreover, for a significant portion of the parameter space, the growth rate on the background critical point 2 is zero.

## 4 Numerical solutions of the perturbation equations

In this section we will illustrate the numerical solutions of the perturbed system of equations (2.8) and (2.9) defined in Section 2 together with the background equations. Our numerical results show a very good agreement with the analysis of Section 3. We will restrict the range of the model's parameters to the stability and acceleration regions of the background critical points of Table 1 [see Ref. 27]. As a first test of our numerical integration, we display in Fig. 2 the total growth function of McDE with  $\alpha = 0.1$  and  $\beta = 0$  (i.e. for the uncoupled case, solid curve) and the growth function  $f_{\Lambda CDM}$  for the standard  $\Lambda$ CDM model given by  $f_{\Lambda CDM} = \Omega_m^\gamma$  with  $\gamma = 0.54$  (dashed curve). The two curves show

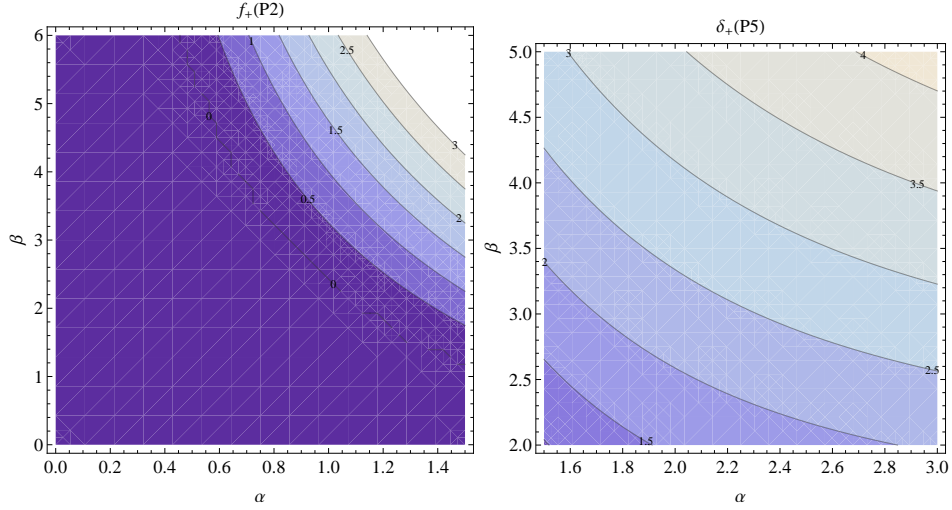


**Figure 1.** *Left panel:* Contour plots of the analytical solution for  $f_+$  for parameters in the stability region of point 2.  $f_-$  is always zero in this region. *Right panel:* The same plot but for the stability region of point 5.

Point	$f_+$	$f_-$	$f$
1	$\max[-\frac{1}{2} - 2\beta, 0]$	$-\frac{1}{2} + 2\beta$ or 0	$f_-$
2	$\max[\frac{1}{3}(-6 + \alpha^2 + 2\alpha\beta), 0]$	$\max[\frac{1}{3}(-6 + \alpha^2 - 2\alpha\beta), 0]$	$f_+$
3	$\max[\frac{1}{4}(-1 + \sqrt{1 + 32\beta^2}), 1]$	$\max[\frac{1}{4}(-1 + \sqrt{1 + 32\beta^2}), 1]$	$f_- + 3$
4	$\frac{1}{12}(-3 - 4\beta^2 + \sqrt{225 - 216\beta^2 - 112\beta^4})$	$\max[f_+, -\frac{1}{2} + 2\beta^2, 0]$	$f_-$
5	$\frac{1}{4}(-1 - \frac{3\beta}{\alpha+\beta}) + \Delta$	$\max[f_+, -5 + \frac{9\alpha}{2(\alpha+\beta)}, 0]$	$f_-$

**Table 2.** Growth functions for each species and total growth function at the background critical points. Here  $\Delta = \sqrt{\frac{4\alpha\beta(5+8\beta^2)+\alpha^2(25+32\beta^2)-4(27+35\beta^2)}{(\alpha+\beta)^2}}$ .

very good agreement, as expected for a standard Quintessence model with a shallow self-interaction potential (indeed the limiting case of  $\alpha = 0, \beta = 0$  exactly corresponds to a  $\Lambda$ CDM cosmology).

As mentioned earlier, we set initial conditions far enough into the past such that the point 4 matter era has already decayed away, leaving only point 3. As we can see in Table 2, on point 3 there are two possible growth rates, unity and  $\frac{1}{4}(-1 + \sqrt{1 + 32\beta^2})$ . Let us now define the initial adiabaticity parameter:

$$A_{\text{ic}} = \frac{\Omega_- \delta_{-i}}{\Omega_+ \delta_{+i}} = \frac{1 - \mu \delta_{-i}}{1 + \mu \delta_{+i}}, \quad (4.1)$$

where  $\mu$  is the asymmetry parameter [see Ref. 25] defined as

$$\mu = \frac{\Omega_+ - \Omega_-}{\Omega_+ + \Omega_-}, \quad (4.2)$$

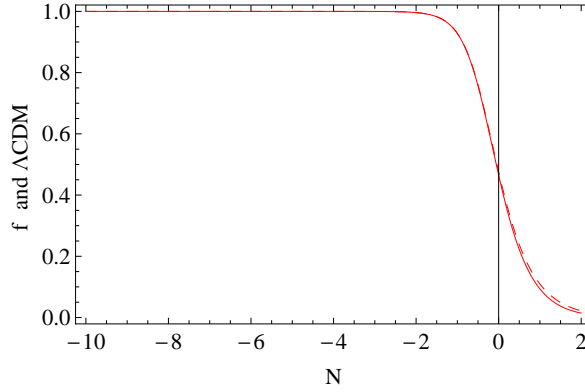


**Figure 2.** Plot of  $f$  (solid curve) when  $\alpha = 0.1$  and  $\beta = 0$ , and of  $f_{\Lambda CDM} = \Omega_m^{0.54}$  (dashed curve).

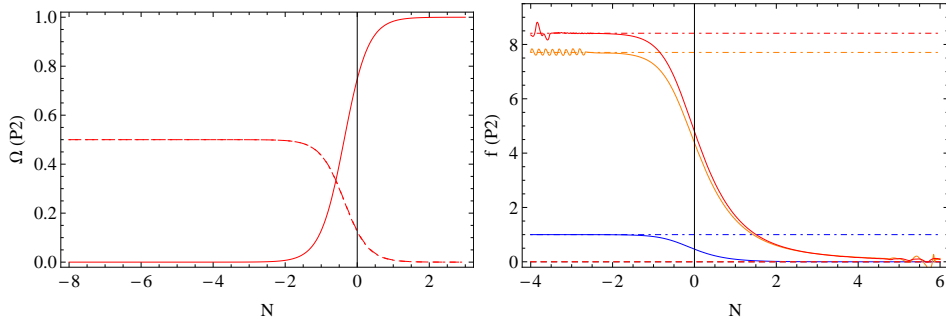


**Figure 3.** The left panel is the plot of  $\Omega_i$  when  $\alpha = 0.1$  and  $\beta = 0.5$ . In this panel, solid curves correspond to  $\Omega_{DE}$  and dashed curves correspond to  $\Omega_-$  and  $\Omega_+$ . The right panel is the plot of  $f$  for  $\alpha = 0.1$  and  $\beta = 0.5$  (blue curve), 3.5 (orange curve), 4 (red curve). The horizontal lines are the analytical values for the matter era (dot-dashed) and the accelerated point 2 (dashed).

and the contrasts  $\delta_{\pm i}$  are evaluated at the initial time. We see that  $A_{ic} = 1$  implies adiabatic initial conditions. We find that if one starts with  $A_{ic} = 1$  at very high redshifts, then initially the growth rate equals unity. However, this trajectory is unstable for  $|\beta| \geq \beta_G = \sqrt{3}/2$  such that soon the growth rate moves to the second value  $\frac{1}{4}(-1 + \sqrt{1 + 32\beta^2})$ . If  $|\beta| < \beta_G$ , instead, the growth rate remains stably at unity. That is, adiabatic fluctuations are unstable, as already found in Ref. [25], for  $|\beta| \geq \beta_G$ . If instead one starts with  $A_{ic}$  substantially different from unity, then the growth rate goes directly to  $\max[1, \frac{1}{4}(-1 + \sqrt{1 + 32\beta^2})]$ .

It is instructive to find the transition point analytically. The full perturbation solutions of point 3 are the following:

$$\delta_+ = \frac{\delta_{+i}}{2} \left[ (1 + A_{ic})e^{f_1(N-N_i)} + (1 - A_{ic})e^{f_2(N-N_i)} \right], \quad (4.3)$$

$$\delta_- = \frac{\delta_{+i}}{2} \left[ (1 + A_{ic})e^{f_1(N-N_i)} - (1 - A_{ic})e^{f_2(N-N_i)} \right], \quad (4.4)$$

where  $A_{ic}$  and  $\delta_{+i}$  are the initial adiabaticity and initial perturbation for the CDM species with positive coupling at  $N_i$ , respectively, and

$$f_1 = 1, \quad f_2 = \frac{1}{4}(-1 + \sqrt{1 + 32\beta^2}). \quad (4.5)$$



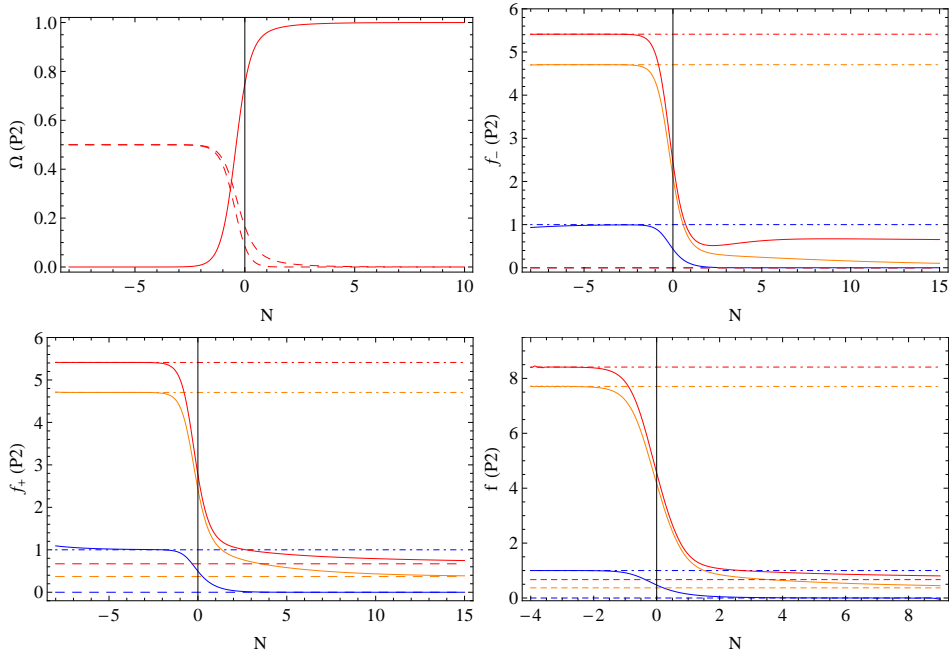


**Figure 4.** The top-left panel is the plot of  $\Omega_i$  when  $\alpha = 0.9$  and  $\beta = 3$ . In this panel, solid curves correspond to  $\Omega_{DE}$  and dashed curves correspond to  $\Omega_-$  and  $\Omega_+$ . The other panels are plots of  $f_-$ ,  $f_+$ ,  $f$  for  $\alpha = 0.9$  and  $\beta = 0.5$  (blue solid curve), 3.5 (orange solid curve), 4 (red solid curve). The dashed horizontal lines are the analytical values for the matter era (dot-dashed) and the accelerated point 2 (dashed).

We can now find the point at which the second term starts to dominate, i.e. the transition time  $N_0$  at which the two terms in eqs. (4.3) and (4.4) are equal. This is given by:

$$N_0 - N_i = \frac{1}{f_2 - f_1} \ln \left| \frac{1 + A_{ic}}{1 - A_{ic}} \right|. \quad (4.6)$$

Therefore, as expected, the transition point  $N_0$  is very close to the initial time  $N_i$ , unless  $A_{ic}$  is extremely close to unity. For instance, when  $\beta = 1$  and the initial adiabaticity is  $A_{ic} = 2$  the transition point occurs 0.5 e-foldings after the initial time and if  $A_{ic} = 1.01$  it occurs after 2.5 e-foldings. The above derivation explicitly shows that adiabatic initial conditions will rapidly evolve into a non-adiabatic state for coupling values  $|\beta| \geq \beta_G$ , while for  $|\beta| < \beta_G$  the initial adiabaticity is preserved. As a consequence, possible observational effects associated with the transition between adiabatic and non-adiabatic initial conditions would be relevant only if the transition occurred in the redshift range covered by observational data, which is a condition that requires a high level of fine-tuning of the model parameters. Therefore, in the following we will restrict to the case of non-adiabatic initial conditions and we will assume  $A_{ic} = 2$ , without loss of generality.

The total growth rate  $f$  is presented in the right panel of Fig. 3 for some values of parameters that lie within the stable range of point 2, comparing with the exact solutions on the critical points. We also present the evolution of background fractional densities for the same values of parameters in the left panel of Fig. 3. For the same values of  $\beta$  but different  $\alpha = 0.9$  we plot the different growth rates  $f_-$ ,  $f_+$ ,  $f$  in the last three panels of Fig. 4. Again, in the first panel of Fig. 4, we illustrate the corresponding evolution of background fractional densities  $\Omega_i$ . We stress here that plots for fractional densities are made for one set of parameters only as the other cases do not differ at the background level. In these two figures, parameters are chosen in the stable range of point 2. Similarly,

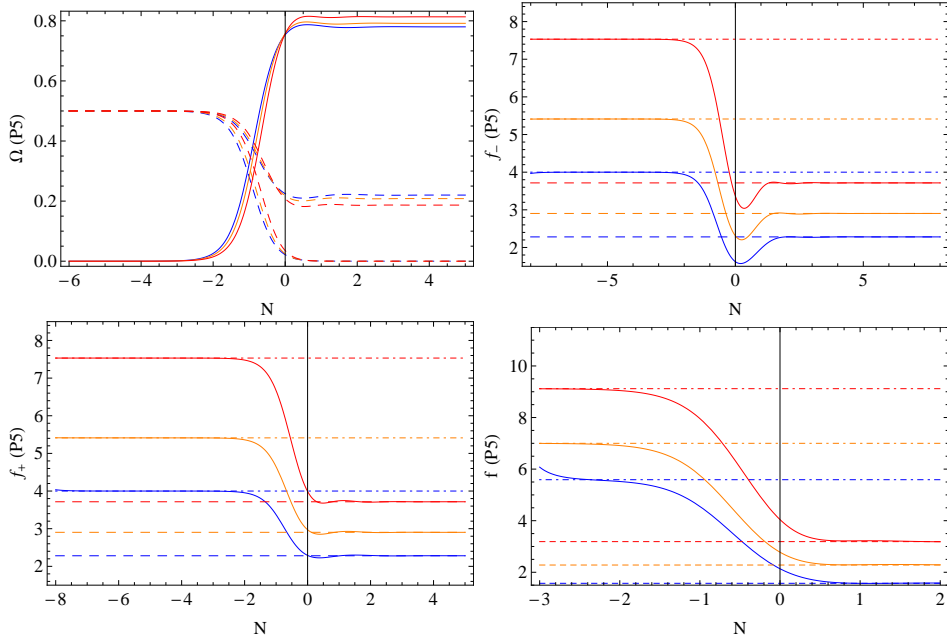


**Figure 5.** As Fig. 4 but for the stable region of point 5.

for parameters within the stable region of point 5, we illustrate the growth rate and the background fractional density evolution in Fig. 5.

The numerical integration of equations (2.8) and (2.9) together with the background equations shows a very interesting effect: during the observationally relevant range  $z \approx 1$ , the growth rate gets strongly enhanced when  $\beta$  grows larger than  $\beta_G$ , before being driven back to a small value when dark energy fully dominates. In Fig. 6 we illustrate this behavior plotting the quantity  $\delta'/\delta_0 = f(z)G(z)$  (where  $G(z)$  is the growth factor normalized to unity today), since this is the observational quantity we will compare our model to in the next section. As can be seen, the McDE behavior suddenly deviates from the  $\Lambda$ CDM case as  $|\beta|$  grows larger than  $\beta_G$ . This leads us to expect that for  $|\beta|$  larger than  $\beta_G$  the model becomes rapidly inconsistent with observations and that growth rate data can place tight constraints on the coupling value, as indeed we are going to find in the next Section.

## 5 Comparison to observations

In our previous work Ref. [27] we employed the Union2.1 Compilation [28] of Type Ia supernovae to constrain the background behavior of the McDE model. We found that supernova data can constrain the slope of the self-interaction potential  $\alpha$ , which is found to be bound to values  $\leq 1.5$  at the  $3\sigma$  confidence level. On the other hand, we found a flat posterior likelihood for the initial asymmetry parameter,  $\mu_{in}$ , which is therefore completely unconstrained by the data, and we derived an extremely loose bound  $|\beta| \lesssim 83$  (at the  $2\sigma$  confidence level) on the coupling parameter. This showed how efficient is the McDE model in mimicking the  $\Lambda$ CDM model at the background level. Here we will extend the previous analysis by confronting the McDE model with present growth rate data as well as forecasted future data from upcoming wide-field surveys: as we will see the study of linear perturbations in the McDE model will allow us to put much tighter constraints on the coupling parameter. We proceed by describing the different data sets entering our investigation, and the likelihood estimator adopted for the comparison with the theoretical predictions.

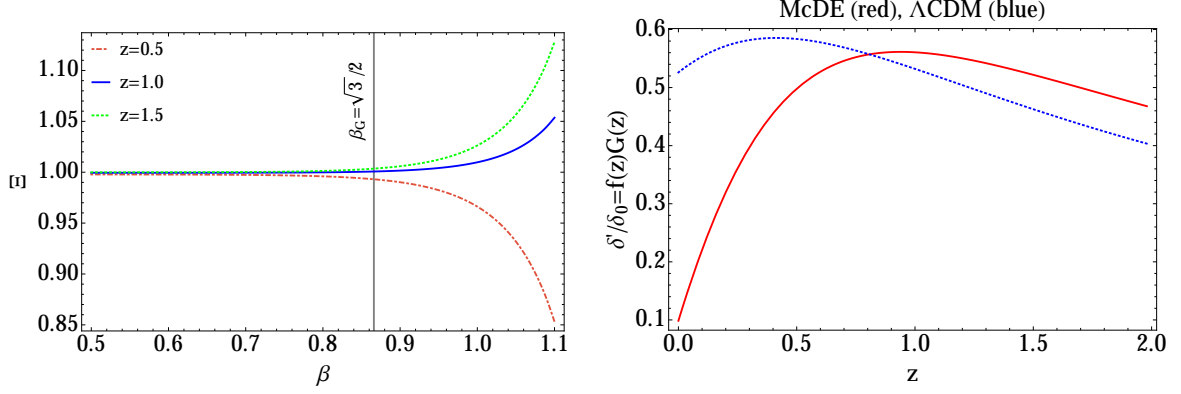


**Figure 6.** *Left Panel:* The ratio  $\Xi \equiv \frac{f(z)G(z)|_{\text{McDE}}}{f(z)G(z)|_{\Lambda\text{CDM}}}$  as a function of the coupling  $\beta$  at  $z = \{0.5, 1, 1.5\}$  and for parameters  $\alpha = 0.1$  and  $\Omega_{\text{DE},0} = 0.692$ . As can be seen, the McDE behavior suddenly deviates from the  $\Lambda$ CDM case as  $|\beta|$  grows larger than  $\beta_G$ . *Right Panel:* evolution with respect to redshift of  $\delta'/\delta_0 = f(z)G(z)$  for the McDE model with  $\beta = 1.1$ ,  $\alpha = 0.1$  and  $\Omega_{\text{DE},0} = 0.692$  (red solid line) and for the  $\Lambda$ CDM model with the same dark-energy content (blue dotted line). The relative trend of the two curves at different redshifts explains the opposite behavior between the  $z = 0.5$  and the  $z \geq 1$  curves shown in the left panel.

## 5.1 SN data

At the background level, we will make use of two different SN datasets. The first is the Union2.1 Compilation [28] of 580 Type Ia SNe in the redshift range  $z = 0.015 - 1.414$ . More precisely, we use the magnitude vs. redshift table (without systematic errors) publicly available at the Supernova Cosmology Project [webpage](#). The second dataset corresponds instead to the forecasted sample of two years of observations by the Large Synoptic Survey Telescope and features a total of  $10^5$  supernovae in the redshift range  $z = 0.1 - 1.0$  with the redshift distribution as given in [32]. We will refer to this dataset at the ‘‘LSST 100k’’ catalog.

The predicted theoretical magnitudes are related to the luminosity distance  $d_L$  by:

$$m(z) = 5 \log_{10} \frac{d_L(z)}{10 \text{ pc}}, \quad (5.1)$$

which is computed under the assumption of spatial flatness:

$$d_L(z) = (1+z) \int_0^z \frac{d\tilde{z}}{H(\tilde{z})}. \quad (5.2)$$

The luminosity distance  $d_L(z)$  is obtained by integrating numerically the background McDE equations as explained in Ref. [27]. The  $\chi^2$  function, on which the likelihood analysis will be based, is then:

$$\chi_{\text{SNIa}}^2 = \sum_i \frac{[m_i - m(z_i) + \xi]^2}{\sigma_i^2}, \quad (5.3)$$

where the index  $i$  labels the elements of the supernova dataset. The parameter  $\xi$  is an unknown offset sum of the supernova absolute magnitudes, of  $k$ -corrections and other possible systematics. As usual, we marginalize the likelihood  $L'_{\text{SNIa}} = \exp(-\chi_{\text{SNIa}}^2/2)$  over  $\xi$ , such that  $L_{\text{SNIa}} = \int d\xi L'_{\text{SNIa}}$ , leading to a new marginalized  $\chi^2$  function:

$$\chi_{\text{SNIa}}^2 = S_2 - \frac{S_1^2}{S_0}, \quad (5.4)$$

where we neglected a cosmology-independent normalizing constant, and the auxiliary quantities  $S_n$  are defined as:

$$S_n \equiv \sum_i \frac{[m_i - m(z_i)]^n}{\sigma_i^2}. \quad (5.5)$$

As  $\xi$  is degenerate with  $\log_{10} H_0$ , we are effectively marginalizing also over the Hubble constant.

## 5.2 $f\sigma_8(z)$ data

At the linear perturbation level, we will build the growth-rate likelihood using two different datasets. The first contains the latest data [see 33] from 6dFGS [34], LRG [35], BOSS [36], WiggleZ [37] and VIPERS [38]. The second dataset approximates instead the forecasted accuracy of a future Euclid-like mission and it has been obtained in Ref. [39].

These different growth-rate data are given as a set of values  $d_i$  where  $i = \{6\text{dFGS, LRG, BOSS, WiggleZ, VIPERS, Euclid}\}$  and where

$$d = f\sigma_8(z) = f(z)\sigma_8 G(z) = \sigma_8 \delta' / \delta_0. \quad (5.6)$$

Let us denote our theoretical estimates as  $t_i = \delta'_i / \delta_0$ , where  $\delta$  indicates the total density perturbation. We can then build a  $\chi^2$  function that reads:

$$\chi_{f\sigma_8}^2 = (d_i - \sigma_8 t_i) C_{ij}^{-1} (d_j - \sigma_8 t_j), \quad (5.7)$$

where  $C_{ij}$  is the covariance matrix of the data. Since we do not know  $\sigma_8$  and cannot use the standard estimates because they have been obtained assuming the standard  $\Lambda$ CDM model, we need to marginalize the likelihood  $L'_{f\sigma_8} = \exp(-\chi_{f\sigma_8}^2/2)$  over  $\sigma_8$ , such that  $L_{f\sigma_8} = \int d\sigma_8 L'_{f\sigma_8}$ , leading to a new marginalized  $\chi^2$  function:

$$\chi_{f\sigma_8}^2 = S_{20} - \frac{S_{11}^2}{S_{02}}, \quad (5.8)$$

where we neglected a cosmology-independent normalizing constant, and the auxiliary quantities  $S_{nm}$  are defined as:

$$S_{11} = d_i C_{ij}^{-1} t_j, \quad (5.9)$$

$$S_{20} = d_i C_{ij}^{-1} d_j, \quad (5.10)$$

$$S_{02} = t_i C_{ij}^{-1} t_j. \quad (5.11)$$

We are effectively marginalizing also over the initial value of  $\delta_0$  as the latter is degenerate with  $\sigma_8$ .

## 5.3 Full likelihood

The full likelihood is based on the total  $\chi^2$ :

$$\chi_{\text{tot}}^2 = \chi_{SNIa}^2 + \chi_{f\sigma_8}^2, \quad (5.12)$$

which depends on the three main parameters  $\Omega_{\text{DE},0}$ ,  $\alpha$ ,  $|\beta|$  plus other parameters specifying the initial conditions,  $A_{\text{ic}}$ ,  $\mu_{\text{in}}$ ,  $\delta_{\pm,\text{in}}$ ,  $\delta'_{\pm,\text{in}}$ . As discussed above, we will solve the perturbation equations with non-adiabatic initial conditions at very early times:  $A_{\text{ic}} = 2$ . This choice is conservative for coupling values  $|\beta| \geq \beta_{\text{G}}$  since adiabatic initial conditions would affect the observable quantities only in the highly fine-tuned case where the departure from adiabaticity occurs at very recent times, while for  $|\beta| < \beta_{\text{G}}$  any choice of  $A_{\text{ic}}$  is equivalent since adiabaticity is conserved. This together with the fact that we are effectively marginalizing over  $\delta_{\pm,\text{in}}$  implies that the likelihood  $L_{\text{tot}} = \exp(-\chi_{\text{tot}}^2/2)$  depends very weakly on the initial conditions parameters, which we have therefore fixed for convenience to  $A_{\text{ic}} = 2$ ,  $\mu_{\text{in}} = 0$ ,  $\delta'_{+,\text{in}} = \delta_{+,\text{in}} = \exp N_{\text{in}}$ ,  $\delta_{-,\text{in}} = A_{\text{ic}} \frac{1+\mu}{1-\mu} \delta_{+,\text{in}}$ ,  $\delta'_{-,\text{in}} = \delta_{-,\text{in}}$ , consistently with the evolution of perturbations during matter domination.

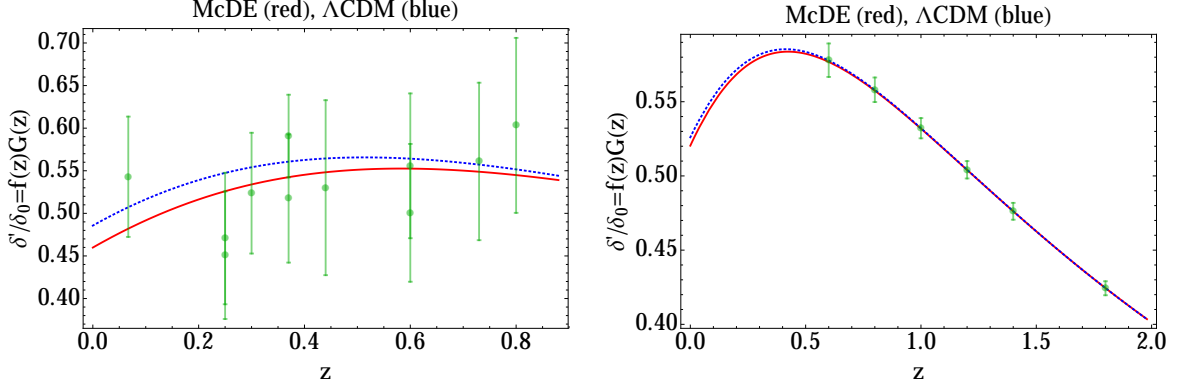


**Figure 7.** Best-fit McDE model (second and fourth columns of Table 3 for left and right panel, respectively) together with  $f\sigma_8$  data points for present (left panel) and future (right panel) data. The  $\Lambda$ CDM curve is displayed for comparison and is relative to a  $\Lambda$ CDM model with the same  $\Omega_{\text{DE},0}$ . As the likelihood is marginalized over  $\sigma_8$ , a possible vertical shift is inconsequential.

Parameter	Best Fit (SN+ $f\sigma_8$ )	95% c.l.	Best Fit (LSST+Euclid)	95% c.l.	Best Fit (SN)	95% c.l.
$\Omega_{\text{DE},0}$	0.734	[0.684, 0.824]	0.692	[0.688, 0.698]	0.719	[0.680, 0.765]
$\alpha$	0.66	[0, 1.36]	0.12	[0, 0.54]	0.62	[0, 1.01]
$\beta$	0.79	[0, 0.88]	0.03	[0, 0.85]	6.4	[0, 83]

**Table 3.** Best-fit values and 95% confidence intervals for the parameters of the model discussed in this paper (for point 2 and point 5 together) when using the combined Union2.1 supernova dataset and the latest  $f\sigma_8$  data (2<sup>st</sup> and 3<sup>rd</sup> columns), or using the combined LSST 100k supernova dataset and the forecasted Euclid-like  $f\sigma_8$  data (4<sup>rd</sup> and 5<sup>th</sup> columns), while the 6<sup>th</sup> and 7<sup>th</sup> columns report the results from [27] when using only background observables and analyzing only point 2.

## 6 Results

The results obtained with the Union2.1 supernova dataset (see Section 5.1) and the latest  $f\sigma_8$  data (see Section 5.2) are shown in Fig. 7 (left panel), Fig. 8 and in the 2<sup>nd</sup> and 3<sup>rd</sup> columns of Table 3. The best-fit values reported in the latter are relative to the full 3-dimensional likelihood. The last two columns of Table 3 report the constraints obtained in [27] when using only background data. As we can see, the effect of including growth rate data in the analysis is dramatic: the  $2\sigma$  confidence region for the coupling  $|\beta|$  shrinks from  $|\beta| \lesssim 83$  when using supernovae only to  $|\beta| \lesssim 0.88$  when present growth rate data is included. This is indeed expected, since one of the main motivations for the introduction of the McDE model was to explore a case in which the  $\Lambda$ CDM expansion is followed closely while the perturbations deviate significantly and show new effects.

The results of the combined LSST 100k supernova dataset (see Section 5.1) and the forecasted Euclid-like  $f\sigma_8$  data (see Section 5.2) are shown in Fig. 7 (right panel), Fig. 9 and in the 4<sup>th</sup> and 5<sup>th</sup> columns of Table 3. These two forecasted catalogs are relative to a  $\Lambda$ CDM fiducial cosmology, using the best-fit cosmological parameters from the Planck Collaboration [40, Table 5, last column]. As we can see in the plots of Fig. 9, with such kind of data we expect to improve constraints on all parameters with respect to present-day data. The 95% limit on  $\alpha$  is reduced by more than a

factor of 2. The 95% constraint on  $|\beta|$  is instead only marginally improved. This shows how McDE models might be difficult to constrain even with the exquisite quality of future Euclid-like data. The constraints on  $|\beta|$  are not strongly improved because the deviation of the McDE growth rate with respect to the  $\Lambda$ CDM one does not scale linearly with  $\beta$ , but it has a step-like behavior, as displayed in Fig. 6, which shows indeed that the McDE growth rate mimics the  $\Lambda$ CDM model for  $|\beta| \lesssim \beta_G$ , but departs from it for larger  $|\beta|$  values. It is therefore very difficult to constrain the coupling parameter to values smaller than  $|\beta| \sim \beta_G$ . Nonlinear clustering data may prove necessary to further constrain McDE models. In particular, a first analysis of the nonlinear evolution of structures within a McDE scenario has been attempted in [31], highlighting for the first time very specific effects like the halo fragmentation process and a peculiar shape of the distortion of the matter power spectrum at small scales. A more detailed investigation of such effects with higher-resolution N-body simulations is presently ongoing, and will be discussed in an upcoming paper.

## 7 Conclusions

The Multi-coupled Dark Energy model has been recently proposed as a simple extension of the standard coupled Quintessence scenario with the intriguing feature of showing an effective screening of the interaction between Dark Energy and Cold Dark Matter particles, without requiring additional free parameters. As a consequence of such screening, the background evolution of the universe closely follows the standard  $\Lambda$ CDM expansion history even for very large values of the coupling constant. This effect makes the Multi-coupled Dark Energy scenario an ideal benchmark to test the discriminating power of present and future multi-probe observational surveys since it maximises the degeneracy with the standard cosmological model in all probes that test only the background cosmic evolution. In a previous paper [27] we have quantified such degeneracy by comparing the predicted expansion history of Multi-coupled Dark Energy models with real observational data consisting of the recent Union2.1 Compilation [28] of Type Ia supernovae, confirming that the background expansion history has a very low constraining power with respect to this scenario. The present paper represents the natural extension of the analysis performed in our previous work to the linear evolution of density perturbations, which are expected to show new physics because of the attractive and repulsive fifth-forces acting between Cold Dark Matter particles, a consequence of their individual coupling to the Dark Energy field.

In order to compare the predicted behavior of linear density perturbations with both presently available and future forecasted data on the growth of structures, we have first derived the full system of perturbed dynamical equations at first order for a generic Multi-coupled Dark Energy cosmology, and analytically solved such set of equations on the few particular background solutions that we had identified as phase-space critical points of the system in our previous work. This has allowed us to obtain the exact solution for the linear growth rate in both the past matter-dominated epoch and future Dark Energy-dominated regime.

Then, we have numerically computed the full solution of linear perturbation equations along the whole expansion history of the universe, for a wide range of model parameters, and compared the numerical solutions with the analytical ones in the appropriate regimes, finding excellent matching between the two. With our numerical solver at hand we have then performed a likelihood analysis by sampling the model's parameter space and comparing the derived evolution with recent observational data of the growth rate, including data sets from 6dFGRS, LRG, BOSS, WiggleZ and VIPERS, as well as with future data consistent with the forecasted accuracy of the Euclid satellite. Our analysis has shown that – as expected – the growth of density perturbations can strongly constrain Multi-coupled Dark Energy scenarios, putting tight bounds on the coupling constant which is constrained

to  $|\beta| \lesssim 0.88$  and  $|\beta| \lesssim 0.85$  at 95% confidence level when considering present and future data sets, respectively.

Interestingly, we have also found that the evolution of linear density perturbations encoded by the growth rate shows a sharp deviation from the standard  $\Lambda$ CDM evolution when the coupling constant  $|\beta|$  approaches and overcomes a critical value  $\beta_G = \sqrt{3}/2$ , corresponding to the coupling value that determines fifth-forces with the same strength as standard gravitational interactions. Nonetheless, as our 95% confidence levels on the coupling directly show, presently available data at the linear level are not yet capable of excluding a coupling value of  $|\beta| = \beta_G$ , and therefore cannot rule out scalar interactions of gravitational strength in the context of a Multi-coupled Dark Energy framework. The natural further extension of this analysis is then to investigate the effects of the Multi-coupled Dark Energy scenario in the nonlinear regime of structure formation by means of dedicated high-resolution N-body simulations, in order to highlight possible characteristic footprints of the model that might allow to further tighten its viable parameter space. Such task is ongoing and will be discussed in an upcoming dedicated paper.

## Acknowledgements

L.A. and V.M. acknowledge financial support from DFG through the project TRR33 "The Dark Universe". M.B. is supported by the Marie Curie Intra European Fellowship "SIDUN" within the 7th Framework Programme of the European Commission. A.P. thanks DAAD for support.

## A Including a baryonic component

### A.1 Equations

We will now consider the case in which, besides dark matter, there is also a baryonic component which does *not* couple to dark energy. We will fix the baryonic content of the universe to the best-fit value  $\Omega_{b,0} = 0.048$  from the Planck Collaboration [40, Table 5, last column]. The background equations will be modified as follows:

$$2\frac{H'}{H} = -(3 - 3y^2 + 3x^2 + r^2), \quad (\text{A.1})$$

$$x' = -x\frac{H'}{H} - 3x + \alpha y^2 + \beta(z_2^2 - z_1^2), \quad (\text{A.2})$$

$$y' = -y\frac{H'}{H} - \alpha xy, \quad (\text{A.3})$$

$$z'_+ = -z_+\frac{H'}{H} - \frac{3}{2}z_+ + \beta x z_+, \quad (\text{A.4})$$

$$z'_- = -z_-\frac{H'}{H} - \frac{3}{2}z_- - \beta x z_-, \quad (\text{A.5})$$

$$r' = -r\frac{H'}{H} - 2r, \quad (\text{A.6})$$

$$z'_b = -z_b\frac{H'}{H} - \frac{3}{2}z_b, \quad (\text{A.7})$$

where

$$z_b^2 \equiv \frac{\rho_b}{3M_{\text{Pl}}^2 H^2}. \quad (\text{A.8})$$



Point	$x$	$y$	$z_+$	$z_-$	$z_b$	$\Omega_{\text{DE}}$	$w_{\text{eff}}$	$\mu$
6	0	0	$\sqrt{\frac{1-z_b^2}{2}}$	$\sqrt{\frac{1-z_b^2}{2}}$	$z_b$	0	0	0
7	$\frac{3}{2\alpha}$	$\frac{3}{2\alpha}$	0	0	$\sqrt{1 - \frac{9}{2\alpha^2}}$	$\frac{9}{2\alpha^2}$	0	0

**Table 4.** Additional critical points for background equations (A.1)-(A.7) when uncoupled baryons are included. Only the physical solutions for  $x, y, z_+, z_-, z_b$  are selected.

Point	$f_+$	$f_-$	$f$	$f_b$
6	$f$	$f$	$\frac{1}{4} \left( -1 + \sqrt{1 + 64z_{cr}^2\beta^2} \right) + 3$	1
7	-	-	$\frac{1}{4} \left( -1 + \sqrt{25 + \frac{108}{\alpha^2}} \right)$	$\frac{1}{4} \left( -1 + \sqrt{25 + \frac{108}{\alpha^2}} \right)$

**Table 5.** Growth functions for additional critical points presented in Table 4.

The additional critical points, present when  $\Omega_b \neq 0$ , are listed in Table 4. The linear perturbation equations, including baryons, read now:

$$\delta_-'' + (2(1 + \beta x) - \frac{1}{2}(3 - 3y^2 + 3x^2 + r^2))\delta_-' = \frac{3}{2}(z_-^2\Gamma_A\delta_- + z_+^2\Gamma_R\delta_+ + z_b^2\delta_b), \quad (\text{A.9})$$

$$\delta_+'' + (2(1 - \beta x) - \frac{1}{2}(3 - 3y^2 + 3x^2 + r^2))\delta_+' = \frac{3}{2}(z_-^2\Gamma_R\delta_- + z_+^2\delta_+\Gamma_A + z_b^2\delta_b), \quad (\text{A.10})$$

$$\delta_b'' + (2 - \frac{1}{2}(3 - 3y^2 + 3x^2 + r^2))\delta_b' = \frac{3}{2}(z_-^2\delta_- + z_+^2\delta_+ + z_b^2\delta_b). \quad (\text{A.11})$$

The analytical solutions for the new background critical points are listed in Table 5. We plot the fractional densities for the new point 2 in the left panel of Fig.10, while in the right panel we display the numerical solutions for  $f$  (solid curves) and its analytical predictions in matter domination (dot-dashed) and DE domination (dashed). The matter point 3 is modified by the additional non-zero  $\Omega_b$ . For instance, in the matter era the dot-dashed curve shows  $\Omega_b = 0.2$  and  $\Omega_{\pm} = 0.4$  (dashed curve) instead of  $\Omega_{\pm} = 0.5$ . The growing solution found for the new critical point 6 in the matter era provided in Table 4 is  $f = 1$  or  $\frac{1}{4} \left( -1 + \sqrt{1 + 64z_{cr}^2\beta^2} \right) + 3$  where  $z_{cr}$ , defined as  $z_{cr} = \sqrt{\frac{1-z_{bI}^2}{2}}$ , corresponds to the fractional density of each CDM species in the matter era, with  $z_{bI}$  the initial baryonic fractional density. Note that the additional 3 in the expression  $\frac{1}{4} \left( -1 + \sqrt{1 + 64z_{cr}^2\beta^2} \right) + 3$  appears for the same reason as explained in Section 3. This growing rate, in the previous case with no baryonic component (corresponding to  $z_{cr} = \frac{\sqrt{2}}{2}$ ) goes back to the old solution (i.e. the present point 6 in Table 4 goes back to the previous point 3 in Table 1 in the appropriate limit). One can also see the differences between the numerical solutions with and without baryons by comparing Fig. 10 with Fig. 3.

## A.2 Results

The results of the combined Union2.1 supernova dataset (see Section 5.1) and the latest  $f\sigma_8$  data (see Section 5.2) for the case of  $\Omega_{b,0} = 0.048$  are shown in Fig 11 and in Table 6 (2<sup>nd</sup> and 3<sup>rd</sup> columns). The results of the combined LSST 100k supernova dataset (see Section 5.1) and the forecasted Euclid-like  $f\sigma_8$  data (see Section 5.2) for the case of  $\Omega_{b,0} = 0.048$  are shown in Fig. 12 and in Table 6 (4<sup>th</sup>



Parameter	Best Fit (SN+ $f\sigma_8$ )	95% c.l.	Best Fit (LSST+Euclid)	95% c.l.	Best Fit (SN)	95% c.l.
$\Omega_{\text{DE},0}$	0.734	[0.684, 0.826]	0.692	[0.688, 0.698]	0.719	[0.680, 0.765]
$\alpha$	0.66	[0, 1.37]	0.12	[0, 0.54]	0.62	[0, 1.01]
$\beta$	0.88	[0, 0.98]	0.03	[0., 0.93]	6.4	[0, 83]

**Table 6.** As Table 3 but for the case where the uncoupled baryonic fraction is also included.

and 5<sup>th</sup> columns). The last two columns of Table 6 report the constraints from [27] obtained by using only background data. In both cases, the constraints on the model parameters  $\Omega_{\text{DE},0}$ ,  $\alpha$  are basically unchanged, while the constraints on the coupling  $\beta$  are slightly weakened, but without substantial modification. This is expected since in the limit where all matter is composed of uncoupled baryons, the value of  $|\beta|$  becomes obviously irrelevant.

## References

- [1] **Supernova Search Team** Collaboration, A. G. Riess *et. al.*, *Observational Evidence from Supernovae for an Accelerating Universe and a Cosmological Constant*, *Astron. J.* **116** (1998) 1009–1038, [[astro-ph/9805201](#)].
- [2] **Supernova Cosmology Project** Collaboration, S. Perlmutter *et. al.*, *Measurements of Omega and Lambda from 42 High-Redshift Supernovae*, *Astrophys. J.* **517** (1999) 565–586, [[astro-ph/9812133](#)].
- [3] **Supernova Search Team** Collaboration, B. P. Schmidt *et. al.*, *The High Z supernova search: Measuring cosmic deceleration and global curvature of the universe using type Ia supernovae*, *Astrophys. J.* **507** (1998) 46–63, [[astro-ph/9805200](#)].
- [4] **The SNLS** Collaboration, P. Astier *et. al.*, *The Supernova Legacy Survey: Measurement of  $\Omega_M$ ,  $\Omega_\Lambda$  and  $w$  from the First Year Data Set*, *Astron. Astrophys.* **447** (2006) 31–48, [[astro-ph/0510447](#)].
- [5] C. P. Ahn, R. Alexandroff, C. Allende Prieto, F. Anders, S. F. Anderson, T. Anderton, B. H. Andrews, É. Aubourg, S. Bailey, F. A. Bastien, and *et al.*, *The Tenth Data Release of the Sloan Digital Sky Survey: First Spectroscopic Data from the SDSS-III Apache Point Observatory Galactic Evolution Experiment*, *arXiv:1307.7735* (July, 2013) [[arXiv:1307.7735](#)].
- [6] **Dark Energy Survey** Collaboration, T. Abbott *et. al.*, *The dark energy survey*, *arXiv:astro-ph/0510346* (2005) [[astro-ph/0510346](#)].
- [7] Z. Ivezic *et. al.*, *LSST: from Science Drivers to Reference Design and Anticipated Data Products*, *arXiv:0805.2366* (2008) [[arXiv:0805.2366](#)].
- [8] R. Laureijs, J. Amiaux, S. Arduini, J. Auguères, J. Brinchmann, R. Cole, M. Cropper, C. Dabin, L. Duvet, A. Ealet, and *et al.*, *Euclid Definition Study Report*, *arXiv:1110.3193* (Oct., 2011) [[arXiv:1110.3193](#)].
- [9] C. Wetterich, *Cosmology and the Fate of Dilatation Symmetry*, *Nucl. Phys.* **B302** (1988) 668.
- [10] B. Ratra and P. J. E. Peebles, *Cosmological Consequences of a Rolling Homogeneous Scalar Field*, *Phys. Rev.* **D37** (1988) 3406.
- [11] C. Armendariz-Picon, V. F. Mukhanov, and P. J. Steinhardt, *Essentials of k-essence*, *Phys. Rev.* **D63** (2001) 103510, [[astro-ph/0006373](#)].

- [12] R. Caldwell, *A Phantom menace?*, *Phys.Lett.* **B545** (2002) 23–29, [[astro-ph/9908168](#)].
- [13] B. Feng, X.-L. Wang, and X.-M. Zhang, *Dark energy constraints from the cosmic age and supernova*, *Phys.Lett.* **B607** (2005) 35–41, [[astro-ph/0404224](#)].
- [14] C. Wetterich, *The Cosmon model for an asymptotically vanishing time dependent cosmological 'constant'*, *Astron. Astrophys.* **301** (1995) 321–328, [[hep-th/9408025](#)].
- [15] L. Amendola, *Coupled quintessence*, *Phys. Rev.* **D62** (2000) 043511, [[astro-ph/9908023](#)].
- [16] G. R. Farrar and P. J. E. Peebles, *Interacting Dark Matter and Dark Energy*, *ApJ* **604** (Mar., 2004) 1–11, [[astro-ph/](#)].
- [17] M. Baldi, *Time-dependent couplings in the dark sector: from background evolution to non-linear structure formation*, *MNRAS* **411** (Feb., 2011) 1077–1103, [[arXiv:1005.2188](#)].
- [18] L. Amendola, M. Baldi, and C. Wetterich, *Quintessence cosmologies with a growing matter component*, *Phys. Rev. D* **78** (July, 2008) 023015, [[arXiv:0706.3064](#)].
- [19] H. A. Buchdahl, *Non-linear Lagrangians and cosmological theory*, *MNRAS* **150** (1970) 1.
- [20] A. A. Starobinsky, *A new type of isotropic cosmological models without singularity*, *Phys. Lett.* **B91** (1980) 99–102.
- [21] W. Hu and I. Sawicki, *Models of  $f(R)$  Cosmic Acceleration that Evade Solar-System Tests*, *Phys. Rev.* **D76** (2007) 064004, [[arXiv:0705.1158](#)].
- [22] T. P. Sotiriou and V. Faraoni,  *$f(R)$  Theories Of Gravity*, *Rev.Mod.Phys.* **82** (2010) 451–497, [[arXiv:0805.1726](#)].
- [23] G. Dvali, G. Gabadadze, and M. Porrati, *4-D gravity on a brane in 5-D Minkowski space*, *Phys.Lett.* **B485** (2000) 208–214, [[hep-th/0005016](#)].
- [24] A. Nicolis, R. Rattazzi, and E. Trincherini, *The Galileon as a local modification of gravity*, *Phys.Rev.* **D79** (2009) 064036, [[arXiv:0811.2197](#)].
- [25] M. Baldi, *Multiple dark matter as a self-regulating mechanism for dark sector interactions*, *Annalen der Physik* **524** (Oct., 2012) 602–617, [[arXiv:1204.0514](#)].
- [26] A. W. Brookfield, C. van de Bruck, and L. M. H. Hall, *New interactions in the dark sector mediated by dark energy*, *Phys. Rev.* **D77** (2008) 043006, [[arXiv:0709.2297](#)].
- [27] A. Piloyan, V. Marra, M. Baldi, and L. Amendola, *Supernova constraints on Multi-coupled Dark Energy*, *JCAP* **07** (2013) 042, [[arXiv:1305.3106](#)].
- [28] N. Suzuki, D. Rubin, C. Lidman, G. Aldering, R. Amanullah, *et. al.*, *The Hubble Space Telescope Cluster Supernova Survey: V. Improving the Dark Energy Constraints Above  $z > 1$  and Building an Early-Type-Hosted Supernova Sample*, *Astrophys.J.* **746** (2012) 85, [[arXiv:1105.3470](#)].
- [29] V. Pettorino, *Testing modified gravity with Planck: the case of coupled dark energy*, *Phys. Rev. D* **88**, **063519** (2013) [[arXiv:1305.7457](#)].
- [30] J.-Q. Xia, *New Limits on Coupled Dark Energy from Planck*, *JCAP* **1311** (2013) 022, [[arXiv:1311.2131](#)].
- [31] M. Baldi, *Structure formation in multiple dark matter cosmologies with long-range scalar interactions*, *MNRAS* **428** (Jan., 2013) 2074–2084, [[arXiv:1206.2348](#)].
- [32] **LSST Science Collaborations, LSST Project Collaboration**, P. A. Abell *et. al.*, *LSST Science Book, Version 2.0*, [arXiv:0912.0201](#).
- [33] E. Macaulay, I. K. Wehus, and H. K. Eriksen, *A Lower Growth Rate from Recent Redshift Space Distortions than Expected from Planck*, [arXiv:1303.6583](#).
- [34] F. Beutler, C. Blake, M. Colless, D. H. Jones, L. Staveley-Smith, *et. al.*, *The 6dF Galaxy Survey:  $z \approx 0$  measurement of the growth rate and  $\sigma_{8}$* , *Mon.Not.Roy.Astron.Soc* **423** (2012) 3430–3444,

[arXiv:1204.4725].

- [35] L. Samushia, W. J. Percival, and A. Raccanelli, *Interpreting large-scale redshift-space distortion measurements*, *Mon.Not.Roy.Astron.Soc.* **420** (2012) 2102–2119, [arXiv:1102.1014].
- [36] R. Tojeiro, W. Percival, J. Brinkmann, J. Brownstein, D. Eisenstein, *et. al.*, *The clustering of galaxies in the SDSS-III Baryon Oscillation Spectroscopic Survey: measuring structure growth using passive galaxies*, *Mon.Not.Roy.Astron.Soc* **424** (2012) 2339–2344, [arXiv:1203.6565].
- [37] C. Blake, S. Brough, M. Colless, C. Contreras, W. Couch, *et. al.*, *The WiggleZ Dark Energy Survey: Joint measurements of the expansion and growth history at  $z < 1$* , *Mon.Not.Roy.Astron.Soc.* **425** (2012) 405–414, [arXiv:1204.3674].
- [38] S. de la Torre, L. Guzzo, J. Peacock, E. Branchini, A. Iovino, *et. al.*, *The VIMOS Public Extragalactic Redshift Survey (VIPERS). Galaxy clustering and redshift-space distortions at  $z=0.8$  in the first data release*, *Astron.Astrophys.* **557** (2013) A54, [arXiv:1303.2622].
- [39] L. Amendola, S. Fogli, A. Guarnizo, M. Kunz, and A. Vollmer, *Model-independent constraints on the cosmological anisotropic stress*, *ArXiv e-prints: arXiv:1311.4765v1* (2013).
- [40] **Planck Collaboration** Collaboration, P. Ade *et. al.*, *Planck 2013 results. XVI. Cosmological parameters*, arXiv:1303.5076.

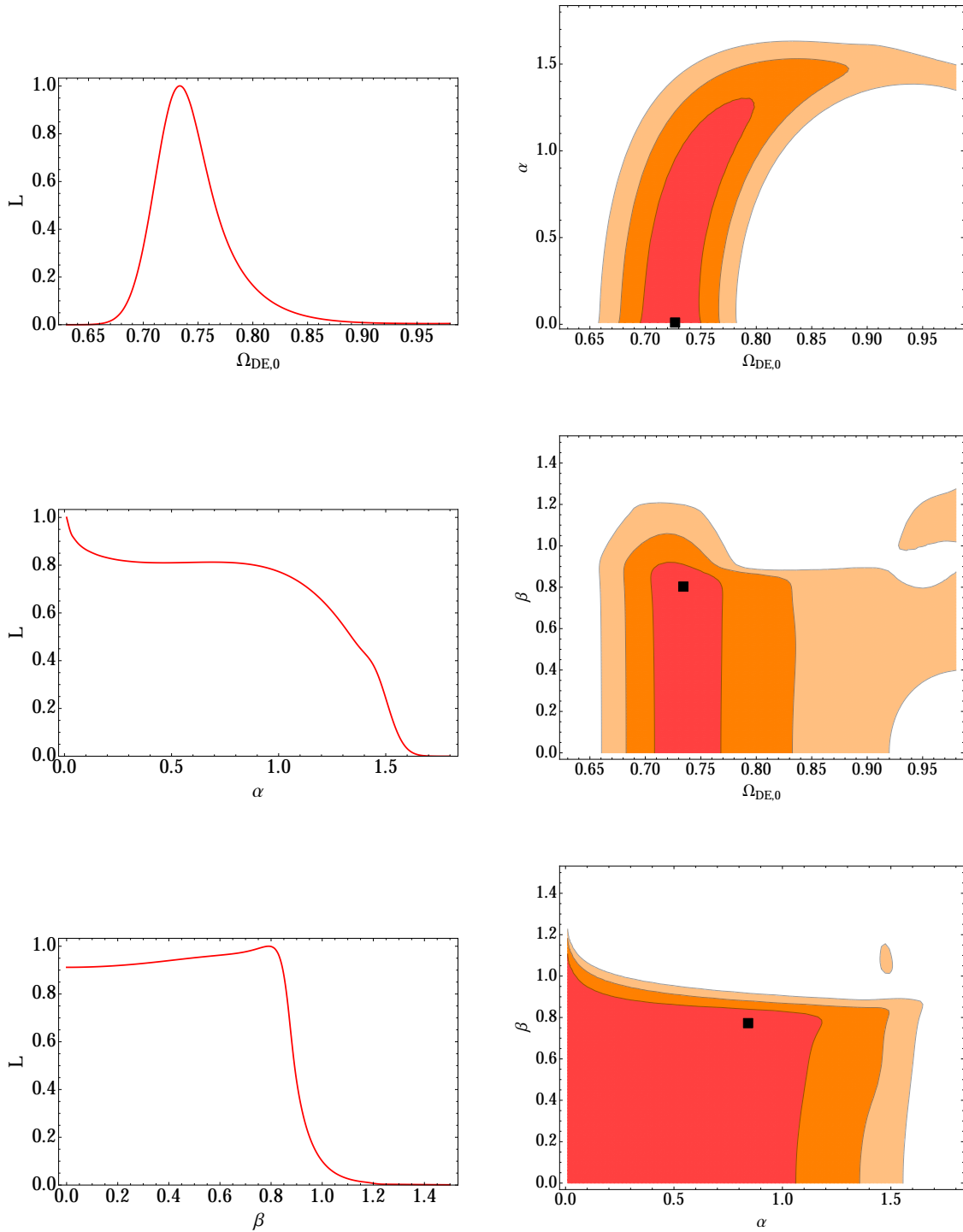


**Figure 8.** *On the Left:* 1-dimensional marginalized posterior distributions (for point 2 and point 5 together) on the parameters  $\{\Omega_{\text{DE},0}, \alpha, \beta\}$  when fitting the model of this paper to the Union2.1 SN Compilation (see Section 5.1) and the latest  $f\sigma_8$  data (see Section 5.2). See second and third columns of Table 3 for best-fit values with 95% confidence intervals. *On the Right:*  $1\sigma$ ,  $2\sigma$  and  $3\sigma$  confidence-level contours for the relevant 2-dimensional marginalized posterior distributions. The black squares mark the best-fit values. The degeneracy between  $\Omega_{\text{DE},0}$  and the parameters  $\alpha, \beta$  makes values of  $\Omega_{\text{DE},0} \simeq 0.90$  possible at the  $3\sigma$  level.

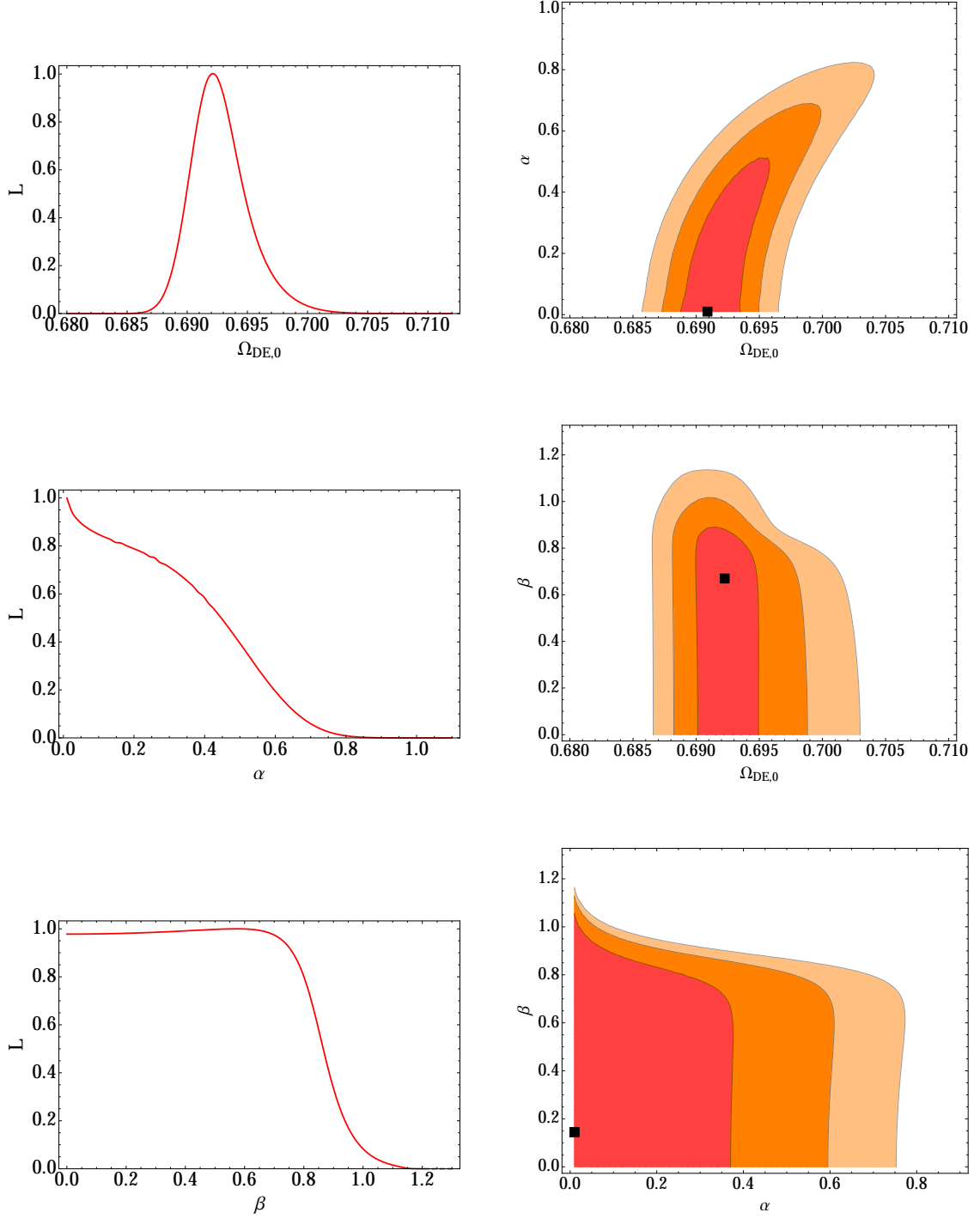


**Figure 9.** *On the Left:* 1-dimensional marginalized posterior distributions (for point 2 and point 5 together) on the parameters  $\{\Omega_{\text{DE},0}, \alpha, \beta\}$  when fitting the model of this paper to the LSST 100k SN dataset (see Section 5.1) and the forecasted Euclid-like  $f\sigma_8$  data (see Section 5.2). See 4<sup>th</sup> and 5<sup>th</sup> columns of Table 3 for best-fit values with 95% confidence intervals. *On the Right:*  $1\sigma$ ,  $2\sigma$  and  $3\sigma$  confidence-level contours for the relevant 2-dimensional marginalized posterior distributions. The black squares mark the best-fit values.

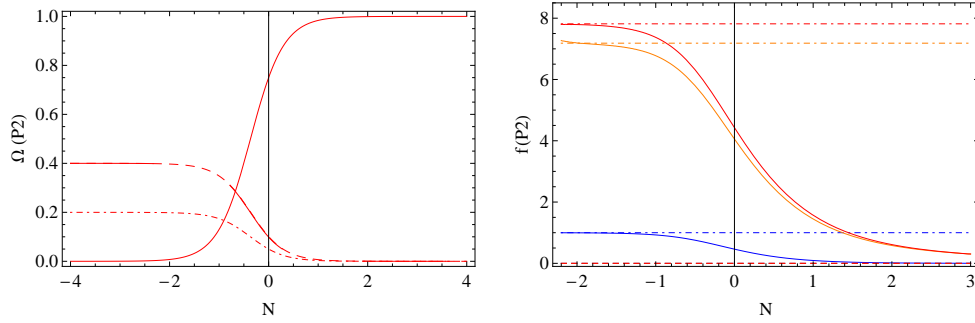


**Figure 10.** *Left panel:* The fractional densities  $\Omega_i$  for  $\alpha = 0.1$  and  $\beta = 0.5$ . Solid curves correspond to  $\Omega_{DE}$ , dot-dashed curves correspond to  $\Omega_b$ , dashed curves correspond to  $\Omega_-$  and  $\Omega_+$ . Parameters are chosen in the stable range of point 2. *Right panel:* The evolution of  $f$  for  $|\beta| = 0.5$  (blue), 3.5 (orange), and 4 (red). The dashed horizontal lines are the analytical values for the matter era and the accelerated point 2.

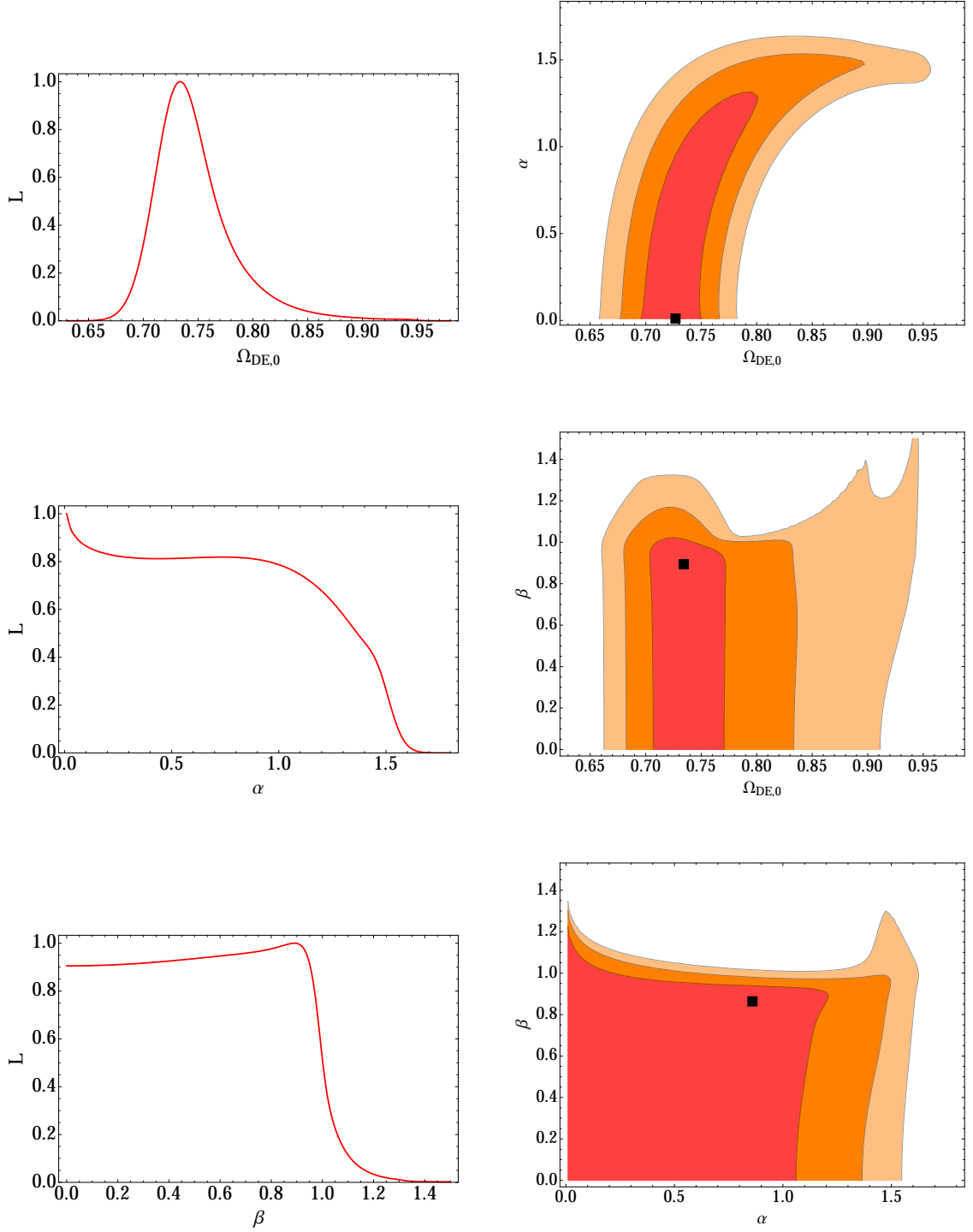


**Figure 11.** *On the Left:* 1-dimensional marginalized posterior distributions (for point 2 and point 5 together) on the parameters  $\{\Omega_{\text{DE},0}, \alpha, \beta\}$  when fitting the model of this paper with  $\Omega_{b,0} = 0.048$  to the Union2.1 SN Compilation (see Section 5.1) and the latest  $f\sigma_8$  data (see Section 5.2). See Table 6 (2<sup>nd</sup> and 3<sup>rd</sup> columns) for best-fit values with 95% confidence intervals. *On the Right:* 1 $\sigma$ , 2 $\sigma$  and 3 $\sigma$  confidence-level contours for the relevant 2-dimensional marginalized posterior distributions. The black squares mark the best-fit values. This plot should be compared to Fig. 8 where the baryonic content has been neglected.

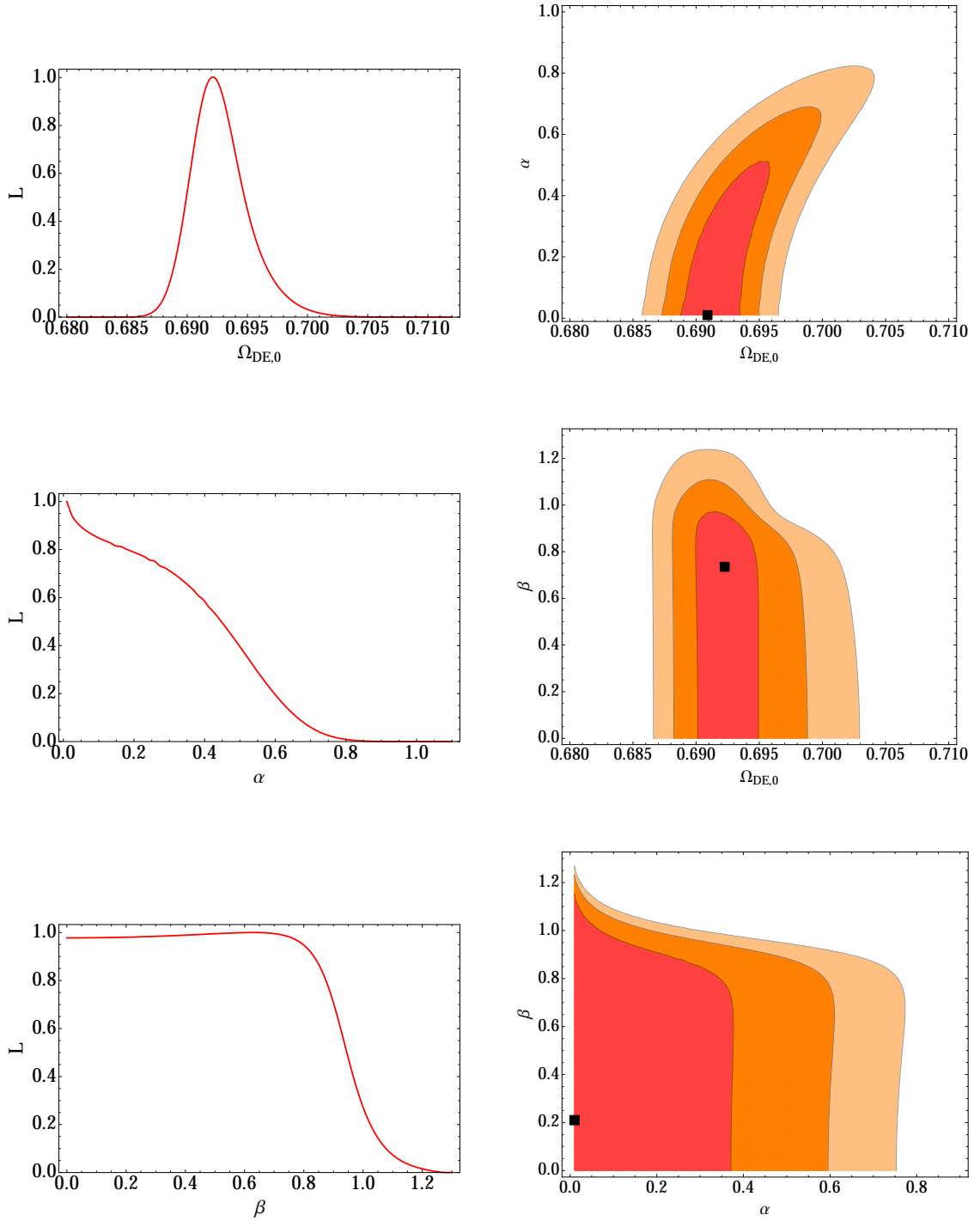


**Figure 12.** *On the Left:* 1-dimensional marginalized posterior distributions (for point 2 and point 5 together) on the parameters  $\{\Omega_{\text{DE},0}, \alpha, \beta\}$  when fitting the model of this paper with  $\Omega_{b,0} = 0.048$  to the LSST 100k SN dataset (see Section 5.1) and the forecasted Euclid-like  $f\sigma_8$  data (see Section 5.2). See Table 6 (4<sup>th</sup> and 5<sup>th</sup> columns) for best-fit values with 95% confidence intervals. *On the Right:* 1 $\sigma$ , 2 $\sigma$  and 3 $\sigma$  confidence-level contours for the relevant 2-dimensional marginalized posterior distributions. The black squares mark the best-fit values. This plot should be compared to Fig. 9 where the baryonic content has been neglected.